Technical Report

TR-2012-009

Iterative Breast Tomosynthesis Image Reconstruction

by

V. Mejia Bustamante, J. G. Nagy, S. Feng, L. Sechopoulos

MATHEMATICS AND COMPUTER SCIENCE

EMORY UNIVERSITY

ITERATIVE BREAST TOMOSYNTHESIS IMAGE RECONSTRUCTION

VERONICA MEJIA BUSTAMANTE*, JAMES G. NAGY[†], STEVE S. J. FENG[‡], AND IOANNIS SECHOPOULOS[§]

Abstract. In digital tomosynthesis imaging, multiple projections of an object are obtained along a small range of different incident angles in order to reconstruct a pseudo-3D representation of the object. In this paper we discuss a mathematical model for polyenergetic digital breast tomosynthesis image reconstruction that explicitly takes into account various materials composing the object and the polyenergetic nature of the x-ray beam. Our model allows for computing weight fractions of the individual materials that make up the object, which can then be used to reconstruct pseudo-3D images. The reconstruction process requires solving a large-scale inverse problem, which is done with a gradient descent iteration. Regularization is enforced by truncating the iteration. The mathematical model is described in detail, as is an efficient approach to compute the gradient of the objective function. The effectiveness of our approach is illustrated with real data taken of an object with known materials that simulates an actual breast.

Key words. digital breast tomosynthesis, iterative methods, gradient descent, iterative regularization, inverse problems, ill-posed problems, beam hardening artifacts

AMS Subject Classifications: 65F22, 65F10, 49N45, 65K99

1. Introduction. Image reconstruction algorithms used, for example, in computed tomography (CT), require solving large-scale inverse problems of the form

$$\boldsymbol{b} = \boldsymbol{K}(\boldsymbol{X})\boldsymbol{s} + \boldsymbol{\eta}\,, \tag{1.1}$$

where $\boldsymbol{b}$ is a vector that contains measured data, $\boldsymbol{K}$ is a matrix that depends on unknown quantities $\boldsymbol{X}$, $\boldsymbol{s}$ is a known vector, and $\boldsymbol{\eta}$ is used to represent errors in the measured data, which can come from electronic noise and scatter. The definition of $\boldsymbol{K}(\boldsymbol{X})$ depends on the specific application, as well as on any simplifying assumptions made for the image formation process. Given $\boldsymbol{b}$, $\boldsymbol{s}$, and a definition for $\boldsymbol{K}$, the aim is to compute an approximation of $\boldsymbol{X}$. It should also be noted that although we may talk about reconstructing and visualizing (displaying) $\boldsymbol{X}$, strictly speaking $\boldsymbol{X}$ is usually not an "image" of an object, but rather it contains information about the object, such as densities.

In this paper we consider discrete inverse problems of the form given by equation (1.1) that arise in a limited angle x-ray tomography technique referred to as *tomosynthesis*, where the function $\boldsymbol{K}(\boldsymbol{X})$ has certain structure that can be exploited when implementing algorithms to solve the inverse problem. The precise structure, and how it can be exploited, depends on how accurately we want to model the physics of the image formation process; this is discussed further in Section 2.

Computing approximations of inverse problems are typically done by formulating an optimization problem involving a fit-to-data term that incorporates regularization

───────

*Department of Mathematics and Computer Science, Emory University. Email: vmejia@emory.edu.

[†]Department of Mathematics and Computer Science, Emory University. Email: nagy@mathcs.emory.edu.

[‡]Department of Biomedical Engineering, Emory University and Georgia Institute of Technology. Email: steven.feng@bme.gatech.edu.

[§]Department of Radiology and Imaging Sciences, and Winship Cancer Institute, Emory University. Email: isechop@emory.edu.

to stabilize the inversion process. The fit-to-data term often takes into account statistical assumptions on the data and noise. In the medical imaging community, it is widely accepted that measurements obtained by x-ray transmission imaging can be accurately modeled as independently distributed Poisson random variables, with additional background noise. We note that it was reported in [17] that no significant difference in reconstructed image quality was noticed when using the Poisson model versus a Gaussian model, but since there is still no published support that one provides superior performance over the other, for this work we use the more widely accepted Poisson model.

In the Poisson statistical model [16], it is assumed that the measured data is a realization of a Poisson random variable, and hence

$$b_k = \text{Poisson}\left([\boldsymbol{K}(\boldsymbol{X})\boldsymbol{s}]_k + \eta_k\right) \quad k = 1, 2, \ldots, N,$$

where b_k, $[\boldsymbol{K}(\boldsymbol{X})\boldsymbol{s}]_k$ and η_k are, respectively, the k-th entries of the vectors $\boldsymbol{b}$, $\boldsymbol{K}(\boldsymbol{X})\boldsymbol{s}$ and $\boldsymbol{\eta}$. The probability, or likeliness, of observing $\boldsymbol{b}$ given $\boldsymbol{X}$ is described by the likelihood function

$$\pi(\boldsymbol{b}\,|\,\boldsymbol{X}) = \prod_{k=1}^{N} \frac{([\boldsymbol{K}(\boldsymbol{X})\boldsymbol{s}]_k + \eta_k)^{b_k} \exp(-([\boldsymbol{K}(\boldsymbol{X})\boldsymbol{s}]_k + \eta_k))}{b_k!}.$$

A fit-to-data term could then be to maximize $\pi(\boldsymbol{b}\,|\,\boldsymbol{X})$, or to minimize the negative of $\ln(\pi(\boldsymbol{b}\,|\,\boldsymbol{X}))$. Ignoring the constant term associated with $b_k!$, we therefore obtain the fit-to-data term

$$\mathcal{L}(\boldsymbol{X}) = \sum_{k=1}^{N} \left(([\boldsymbol{K}(\boldsymbol{X})\boldsymbol{s}]_k + \eta_k) - b_k \ln([\boldsymbol{K}(\boldsymbol{X})\boldsymbol{s}]_k + \eta_k)\right). \qquad (1.2)$$

The image reconstruction problem, especially with limited data, is well known to be ill-posed, and regularization is needed to stabilize the inversion process in the presence of noise. Developing regularization approaches for general nonlinear inverse problems can be significantly more challenging than it is for the linear case. Nevertheless, some general computational approaches have been successful, including iterative regularization and variational approaches [10, 11, 12]. In this paper we use iterative regularization. Specifically, we apply an iterative gradient descent method to minimize $\mathcal{L}(\boldsymbol{X})$, and use a stopping rule to enforce regularization.

The rest of this paper is organized as follows. In Section 2 we describe a general (nonlinear) mathematical model for tomosynthesis imaging that incorporates the polyenergetic nature of the x-ray beam, and we show what simplifications are needed to obtain the standard (linear) model that assumes a monoengergetic x-ray beam. We also describe how the model can incorporate specific information about the materials that make up the object being imaged. In Section 3 we consider an iterative regularization approach, using gradient descent, to solve the polyenergetic tomosynthesis image reconstruction inverse problem. Numerical experiments using real projection data of a phantom breast object, with known materials, are presented in Section 4, and concluding remarks are given in Section 5.

2. Tomosynthesis Imaging. Modern conventional x-ray systems that use digital technology have many benefits to the classical film x-ray systems, including a linear response, improved workflow and decreased re-takes, and somewhat lower radiation dose. The term "conventional" is used to refer to a system that produces a

2-dimensional projection image of a 3-dimensional object, as opposed to computed tomography (CT), which produces 3-dimensional images. Because of their improved response and ease of use, digital x-ray systems are widely used in medicine, from emergency rooms, to mammography, to dentistry. The greatest contribution of the introduction of digital detectors to radiography is the ease of performing image processing on digital images and the ability to use more advanced image acquisition techniques, such as digital tomosynthesis.

Digital tomosynthesis is a technique that can produce 3-dimensional image information of an object using slightly modified conventional digital x-ray systems [7]. The idea underlying tomosynthesis is that multiple 2D image projections of the object are taken at varying incident angles, and each 2D image provides different information about the 3D object. See Figure 2.1 for an illustration of a typical geometry for breast tomosynthesis imaging. See [7] and references therein for a survey of previous approaches to the tomosynthesis image reconstruction problem.
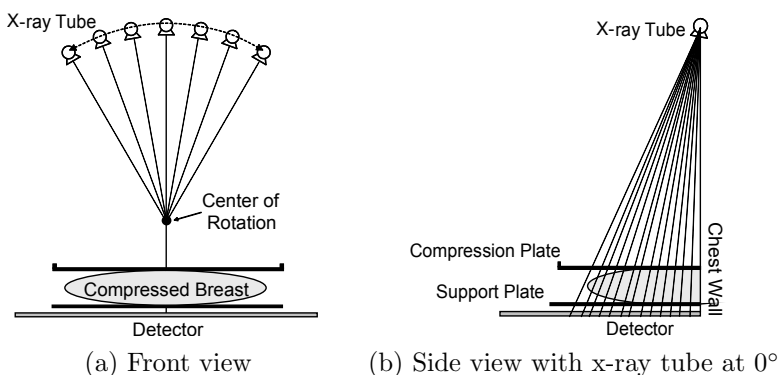

(a) Front view (b) Side view with x-ray tube at 0°

FIG. 2.1. *Typical geometry of a tomosynthesis imaging device used in breast imaging. The illustration on the left shows the x-ray source at 7 different locations.*

2.1. A General Mathematical Model. To describe a mathematical model of the image formation process, let $b_i^{(\theta)}$ be the quantity measured at the i-th pixel of a digital x-ray detector, obtained when the x-ray source is at an incident angle θ. Using Beer's law [13], these measured values are related to the object's attenuation (that is, the fraction of the x-ray absorbed or scattered by the object) through the integral equation

$$b_i^{(\theta)} = \int_\varepsilon s(\varepsilon) e^{-\int_{L_\theta} \mu(\vec{x}, \varepsilon)\, d\ell}\, d\varepsilon + \eta_i^{(\theta)}, \quad i = 1, 2, \ldots, N_p \quad \text{and} \quad \theta = 1, 2, \ldots, N_\theta$$

(2.1)

where
- N_p is the number of pixels (typically a few million) in the digital x-ray detector.
- N_θ is the number of projection images obtained when the x-ray source is moved to a new position, which is defined by an angle θ. In a typical tomosynthesis system $15 \leq N_\theta \leq 30$.
- ε represents the spectrum of energies that are emitted by the source x-ray beam, which can, for example, range from 10 keV to 28 keV.
- $s(\varepsilon)$ is the energy fluence, which is a product of the x-ray energy with the number of incident photons at that energy.

- L_θ is the line on which the x-ray beam travels through the object.
- $\mu(\vec{x}, \varepsilon)$ is the linear attenuation coefficient, which depends on the energy of the x-ray beam and on the material in the object at the position $\vec{x}$; lower energy will be attenuated more than higher energy, and denser materials such as bone or calcifications will attenuate more than soft tissue.
- $\eta_i^{(\theta)}$ represents additional contributions (noise) measured at the detector, which can include x-ray scatter and electronic noise.

Discretizing the integrals in equation (2.1) leads to the discrete image formation model

$$b_i^{(\theta)} = \sum_{\varepsilon=1}^{N_\varepsilon} s_\varepsilon \exp\left(-\sum_{\ell=1}^{N_v} a_{i,\ell}^{(\theta)} \mu_{\ell,\varepsilon}\right) + \eta_i^{(\theta)}, \quad \left\{ \begin{array}{l} i = 1, 2, \ldots, N_p \\ \theta = 1, 2, \ldots, N_\theta \end{array} \right. \tag{2.2}$$

where

- N_v is the number of voxels (typically a few billion) in the discretized 3D object.
- N_ε is the number of discrete energy levels. Because N_v is extremely large, in general $N_\varepsilon \ll N_v$.
- $a_{i,\ell}^{(\theta)}$ is the length of the x-ray that passes through voxel ℓ, contributing to pixel i.

Defining a matrix $\boldsymbol{A}^{(\theta)}$ with entries $a_{i,\ell}^{(\theta)}$ and a matrix $\boldsymbol{\mathcal{M}}$ with entries $\mu_{\ell,\varepsilon}$, equation (2.2) can be written in matrix-vector form as

$$\boldsymbol{b}^{(\theta)} = \exp\left(-\boldsymbol{A}^{(\theta)}\boldsymbol{\mathcal{M}}\right)\boldsymbol{s} + \boldsymbol{\eta}^{(\theta)}, \quad \theta = 1, 2, \ldots, N_\theta \tag{2.3}$$

where the exponentiation operation is done element-wise on the matrix $-\boldsymbol{A}^{(\theta)}\boldsymbol{\mathcal{M}}$. A discrete model that comprises all projections can be written as

$$\boldsymbol{b} = \exp\left(-\boldsymbol{A}\boldsymbol{\mathcal{M}}\right)\boldsymbol{s} + \boldsymbol{\eta} \tag{2.4}$$

where

$$\boldsymbol{b} = \left[\begin{array}{c} \boldsymbol{b}^{(1)} \\ \boldsymbol{b}^{(2)} \\ \vdots \\ \boldsymbol{b}^{(N_\theta)} \end{array}\right] \quad \text{and} \quad \boldsymbol{A} = \left[\begin{array}{c} \boldsymbol{A}^{(1)} \\ \boldsymbol{A}^{(2)} \\ \vdots \\ \boldsymbol{A}^{(N_\theta)} \end{array}\right]$$

We remark that the $N_p \times N_v$ *ray trace* matrices $\boldsymbol{A}^{(\theta)}$ are sparse, but because of the large dimensions involved in a typical application, computer memory can be an issue if they are constructed and stored explicitly, even when using an efficient sparse data format. As previously mentioned, $\boldsymbol{s}$ is a product of the source x-ray energy with the number of incident photons at that energy. An accurate estimate of the x-ray energy distribution can be obtained using well-known x-ray spectra models [5], and calibration measurements can be obtained by taking x-ray transmission measurements of objects (e.g. high-purity aluminum) that have known dimension, density and material composition [15]. Information about the additive noise term, $\boldsymbol{\eta}$, can be also estimated through preprocessing or calibration steps [14].

Using this x-ray spectra modeling, the image reconstruction problem assumes $\boldsymbol{b}$, $\boldsymbol{A}$ and $\boldsymbol{s}$ are known, and it is necessary to solve the inverse problem (2.4) for attenuation

coefficients $\boldsymbol{\mathcal{M}}$, or equivalently we need to solve the general inverse problem (1.1), where

$$K(X) \equiv \exp\left(-AX\right), \quad \text{with} \quad X \equiv \boldsymbol{\mathcal{M}}.$$

It is computationally challenging to solve this nonlinear inverse problem; typically, simplifying assumption are used to get an approximate linear model that is much easier to solve, but may result in unwanted artifacts in the reconstructed image.

2.2. Linear Approximation of the Mathematical Model. In a real imaging system, x-rays emitted from the source are *polyenergetic*, meaning that they are made up of photons having a wide range of energies [13]. But as was described in the previous subsection, an accurate polyenergetic model requires solving a large scale nonlinear inverse problem to compute the attenuation coefficients. With the exception of our recent work [4], all tomosynthesis breast image reconstruction methods assume the source x-rays are *monoenergetic*, which means $N_\varepsilon = 1$, $\boldsymbol{\mathcal{M}}$ is a vector, and s is a scalar. With this simplifying assumption, equation (2.4) is typically rewritten as a linear inverse problem

$$\hat{b} = AX + \eta,$$

where $X \equiv \boldsymbol{\mathcal{M}}$, and the entries of $\hat{b}$ are

$$\hat{b}_i = -\log\left(\frac{b_i}{s}\right).$$

Although it is much easier to solve, there are disadvantages to using a simplified linear model. For example, ignoring the energy dependence in the mathematical model can lead to artifacts in the reconstructed image, apparent in dark streaks near high density objects, such as calcifications. This will be illustrated in our experimental results in Section 4. Few researchers have studied methods for eliminating these so called *beam hardening* artifacts, and then only in the case of whole-body CT [1, 3, 6, 8, 9]. In our previous work [4], we showed that it is possible to remove beam hardening artifacts in tomosynthesis imaging.

In this paper, we consider a new approach that improves on our previous work. First, we generalize the mathematical model for material decomposition, which allows for computing quantitative information about the materials in the object, and it provides a sparse decomposition of the unknown into basis components. Moreover, we describe efficient iterative methods to solve the inverse problem, and we present results using real projection data that clearly shows our approach is superior to existing methods. The rest of this section describes the mathematical model we use for material decomposition.

2.3. Multimaterial Model. In this section we provide a general frame work for material decomposition. This is a generalization of our previous work [4]. First we note that, under the assumption that the densities of different components are similar, the linear attenuation coefficients $\mu_{\ell,\varepsilon}$, of the composite material making the object (e.g., the breast) can be approximated as a linear combination of individual materials. That is, suppose that there are N_m distinct materials making up the object, and that

$$\mu_{\ell,\varepsilon} \approx \sum_{m=1}^{N_m} w_{\ell,m} c_{m,\varepsilon}, \tag{2.5}$$

where

- $c_{m,\varepsilon}$ are known linear attenuation coefficients for the m-th material in voxel ℓ at x-ray energy ε. These coefficients, for a variety of specific materials, can be obtained from [2].
- $w_{\ell,m}$ are unknown weight fractions (or percentages) of the m-th material in the ℓ-th voxel of the object.

We also assume that the weight fractions for each voxel should add to 1 (or percentages should add to 100), which means:

$$\sum_{m=1}^{N_m} w_{\ell,m} = 1\,, \quad \ell = 1, 2, \ldots, N_v$$

or, equivalently,

$$w_{\ell,1} = 1 - \sum_{m=2}^{N_m} w_{\ell,m}\,. \tag{2.6}$$

Substituting relations (2.5) and (2.6) into equation (2.2), we obtain

$$b_i^{(\theta)} = \sum_{\varepsilon=1}^{N_\varepsilon} s_\varepsilon \exp\left(-\sum_{\ell=1}^{N_v} a_{i,\ell}^{(\theta)} \sum_{m=1}^{N_m} w_{\ell,m} c_{m,\varepsilon}\right) + \eta_i^{(\theta)} \tag{2.7}$$

$$= \sum_{\varepsilon=1}^{N_\varepsilon} s_\varepsilon \exp\left(-\sum_{\ell=1}^{N_v} a_{i,\ell}^{(\theta)} \left(c_{1,\varepsilon} + \sum_{m=2}^{N_m} w_{\ell,m}(c_{m,\varepsilon} - c_{1,\varepsilon})\right)\right) + \eta_i^{(\theta)}\,. \tag{2.8}$$

In matrix-vector form, equations (2.7) and (2.8), respectively, can be written as

$$\boldsymbol{b} = \exp\left(-\boldsymbol{A}\boldsymbol{W}\boldsymbol{C}^T\right)\boldsymbol{s} + \boldsymbol{\eta} \tag{2.9}$$

$$= \exp\left(-\boldsymbol{A}\left(\boldsymbol{1}\boldsymbol{c}_1^T + \boldsymbol{X}\widehat{\boldsymbol{C}}^T\right)\right)\boldsymbol{s} + \boldsymbol{\eta}\,. \tag{2.10}$$

In equation (2.9), our notation is as follows:
- $\boldsymbol{C}$ is an $N_\varepsilon \times N_m$ matrix, with entries $c_{\varepsilon,m}$. That is, each column of $\boldsymbol{C}$ contains the known attenuation coefficients of the m-th material.
- $\boldsymbol{W}$ is an $N_v \times N_m$ matrix, with entries $w_{\ell,m}$. That is, each column of $\boldsymbol{W}$ contains the unknown weight fractions of the m-th material.

In equation (2.10), our notation is as follows:
- If we denote the columns of $\boldsymbol{C}$ as $\boldsymbol{c}_1, \boldsymbol{c}_2, \ldots, \boldsymbol{c}_{N_m}$, then $\boldsymbol{c}_1$ is the first column of $\boldsymbol{C}$, and

$$\widehat{\boldsymbol{C}} = \left[\ \boldsymbol{c}_2 - \boldsymbol{c}_1 \ \middle|\ \boldsymbol{c}_3 - \boldsymbol{c}_1 \ \middle|\ \cdots\ \middle|\ \boldsymbol{c}_{N_m} - \boldsymbol{c}_1\ \right]\,.$$

- If we denote the columns of $\boldsymbol{W}$ as $\boldsymbol{w}_1, \boldsymbol{w}_2, \ldots, \boldsymbol{w}_{N_m}$, then we define the unknown in our resulting inverse problems as

$$\boldsymbol{X} = \left[\ \boldsymbol{w}_2 \ \middle|\ \boldsymbol{w}_3 \ \middle|\ \cdots\ \middle|\ \boldsymbol{w}_{N_m}\ \right]\,.$$

Thus, our goal is to solve the general inverse problem (1.1), where

$$\boldsymbol{K}(\boldsymbol{X}) \equiv \exp\left(-\boldsymbol{A}\left(\boldsymbol{1}\boldsymbol{c}_1^T + \boldsymbol{X}\widehat{\boldsymbol{C}}^T\right)\right)\,.$$

3. Iterative Solution of Inverse Problem. Consider the inverse problem,

$$\boldsymbol{b} = \boldsymbol{K}(\boldsymbol{X})\boldsymbol{s} + \boldsymbol{\eta}\,,$$

and recall that a maximum likelihood solution is obtained by minimizing

$$\mathcal{L}(\boldsymbol{X}) = \sum_{k=1}^{N} \left(\left([\boldsymbol{K}(\boldsymbol{X})\boldsymbol{s}]_k + \eta_k\right) - b_k \ln([\boldsymbol{K}(\boldsymbol{X})\boldsymbol{s}]_k + \eta_k)\right)\,, \tag{3.1}$$

where, in our tomosynthesis application, $N = N_p N_\theta$. In this paper we use the gradient descent method to compute a minimum of $\mathcal{L}(\boldsymbol{X})$, and enforce regularization by truncating the iteration. To compute a minimum of $\mathcal{L}(\boldsymbol{X})$, we need to compute the gradient,

$$\nabla \mathcal{L}(\boldsymbol{X}) = \mathrm{vec}\left(\frac{\partial \mathcal{L}}{\partial x_{i,j}}\right)\,,$$

where we can see from equation (3.1) that

$$\frac{\partial \mathcal{L}}{\partial x_{i,j}} = \sum_{k=1}^{N} \left(1 - \frac{b_k}{[\boldsymbol{K}(\boldsymbol{X})\boldsymbol{s}]_k + \eta_k}\right) \frac{\partial}{\partial x_{i,j}}[\boldsymbol{K}(\boldsymbol{X})\boldsymbol{s}]_k\,.$$

As discussed in the previous section, we are interested in considering problems where $\boldsymbol{K}(\boldsymbol{X}) \equiv \exp\left(-\boldsymbol{A}\left(\boldsymbol{1}\boldsymbol{c}_1^T + \boldsymbol{X}\widehat{\boldsymbol{C}}^T\right)\right)$. Thus, to complete our derivative calculations, we need to compute

$$\frac{\partial}{\partial x_{i,j}}\left[\boldsymbol{K}(\boldsymbol{X})\boldsymbol{s}\right]_k = \frac{\partial}{\partial x_{i,j}}\left[\exp\left(-\boldsymbol{A}\left(\boldsymbol{1}\boldsymbol{c}_1^T + \boldsymbol{X}\widehat{\boldsymbol{C}}^T\right)\right)\boldsymbol{s}\right]_k$$

$$= \frac{\partial}{\partial x_{i,j}}\left(\sum_{\varepsilon=1}^{N_\varepsilon}\left[\exp\left(-\boldsymbol{A}\left(\boldsymbol{1}\boldsymbol{c}_1^T + \boldsymbol{X}\widehat{\boldsymbol{C}}^T\right)\right)\right]_{k,\varepsilon}s_\varepsilon\right)$$

$$= -\sum_{\varepsilon=1}^{N_\varepsilon}\left[\exp\left(-\boldsymbol{A}\left(\boldsymbol{1}\boldsymbol{c}_1^T + \boldsymbol{X}\widehat{\boldsymbol{C}}^T\right)\right)\right]_{k,\varepsilon}s_\varepsilon\frac{\partial}{\partial x_{i,j}}\left[\boldsymbol{A}\left(\boldsymbol{1}\boldsymbol{c}_1^T + \boldsymbol{X}\widehat{\boldsymbol{C}}^T\right)\right]_{k,\varepsilon}$$

$$= -\sum_{\varepsilon=1}^{N_\varepsilon}\left[\exp\left(-\boldsymbol{A}\left(\boldsymbol{1}\boldsymbol{c}_1^T + \boldsymbol{X}\widehat{\boldsymbol{C}}^T\right)\right)\right]_{k,\varepsilon}s_\varepsilon a_{k,i}\hat{c}_{\varepsilon,j}$$

$$= -a_{k,i}\sum_{\varepsilon=1}^{N_\varepsilon}\left[\exp\left(-\boldsymbol{A}\left(\boldsymbol{1}\boldsymbol{c}_1^T + \boldsymbol{X}\widehat{\boldsymbol{C}}^T\right)\right)\right]_{k,\varepsilon}s_\varepsilon\hat{c}_{\varepsilon,j}$$

$$= -a_{k,i}\left[\boldsymbol{K}(\boldsymbol{X})(\boldsymbol{s}\odot\hat{\boldsymbol{c}}_j)\right]_k\,.$$

Therefore,

$$\frac{\partial \mathcal{L}}{\partial x_{i,j}} = \sum_{k=1}^{N}\left(1 - \frac{b_k}{[\boldsymbol{K}(\boldsymbol{X})\boldsymbol{s}]_k + \eta_k}\right)\frac{\partial}{\partial x_{i,j}}[\boldsymbol{K}(\boldsymbol{X})\boldsymbol{s}]_k$$

$$= \sum_{k=1}^{N}a_{k,i}\left(\frac{b_k}{[\boldsymbol{K}(\boldsymbol{X})\boldsymbol{s}]_k + \eta_k} - 1\right)[\boldsymbol{K}(\boldsymbol{X})(\boldsymbol{s}\odot\hat{\boldsymbol{c}}_j)]_k$$

$$= \boldsymbol{e}_i^T\boldsymbol{A}^T\left((\boldsymbol{b}\oslash(\boldsymbol{K}(\boldsymbol{X})\boldsymbol{s}+\boldsymbol{\eta})-\boldsymbol{1})\odot(\boldsymbol{K}(\boldsymbol{X})(\boldsymbol{s}\odot\hat{\boldsymbol{c}}_j))\right)$$

where $\hat{\boldsymbol{c}}_j$ is the j-th column of $\widehat{\boldsymbol{C}}$, $\odot$ denotes component wise multiplication, and $\oslash$ denotes component wise division. Thus,

$$\nabla\mathcal{L}(\boldsymbol{X}) = \text{vec}\left(\boldsymbol{A}^T\boldsymbol{V}(\boldsymbol{X})\right)$$

where

$$\boldsymbol{V}(\boldsymbol{X}) = \text{vec}\left(\boldsymbol{A}^T\left[\begin{array}{c|c|c|c} \boldsymbol{v}_1(\boldsymbol{X}) & \boldsymbol{v}_2(\boldsymbol{X}) & \cdots & \boldsymbol{v}_{N_m-1}(\boldsymbol{X}) \end{array}\right]\right)$$

and

$$\boldsymbol{v}_j(\boldsymbol{X}) = ((\boldsymbol{b} \oslash (\boldsymbol{K}(\boldsymbol{X})\boldsymbol{s} + \boldsymbol{\eta}) - \boldsymbol{1}) \odot (\boldsymbol{K}(\boldsymbol{X})(\boldsymbol{s} \odot \hat{\boldsymbol{c}}_j))), \quad j = 1, 2, \ldots, N_m - 1.$$

Although it is possible to compute the Hessian for this problem, we omit the derivation from this paper for two important reasons. First, implementation of a Hessian solve for Newton type methods would be very expensive, and secondly, as we show in our numerical results, because the limited angle information from tomosynthesis causes the problem to be severely ill-posed, a gradient descent method requires relatively few iterations to compute a reasonably accurate regularized solution.

It is difficult to precisely quantify the cost of implementing a gradient descent method for this problem because, for example, the sparsity of $\boldsymbol{A}$ depends on the geometry of the x-ray source and detector. However, a rough idea can be determined by counting the number of matrix-vector multiplications with $\boldsymbol{A}$ and $\boldsymbol{A}^T$ per iteration. A function evaluation, that is computing $\boldsymbol{K}(\boldsymbol{X})\boldsymbol{s}$, requires N_m-1 multiplications with $\boldsymbol{A}$, and computation of the gradient requires an additional N_m-1 multiplications with $\boldsymbol{A}^T$, where N_m is the number of basis materials used to model the object. Recall that $\boldsymbol{A}$ is an $N_pN_\theta \times N_v$ matrix, where N_p is the number of pixels in each measured x-ray projection image, N_θ is the number of obtained projections, and N_v is the number of voxels used for the discretization of the object. We note that the sparsity and structure of each $\boldsymbol{A}^{(\theta)}$ is completely dependent on angle of acquisition, and $\boldsymbol{A}^{(\theta)}$ is neither symmetric nor structurally symmetric. If the object is discretized into $n_x \times n_y \times n_z$ voxels (that is, $N_v = n_xn_yn_z$), then the maximum number of non zeros in a row is $\dfrac{n_x + n_y + n_z}{2}$. With typical values of $n_x = 1280$, $n_y = 2048$, and $n_z = 50$, it is not practical to explicitly construct $\boldsymbol{A}^{(\theta)}$. However, matrix-vector multiplications with $\boldsymbol{A}$ and $\boldsymbol{A}^T$ can be implemented efficiently with function calls. Moreover, we remark that we have a very efficient parallel implementation of the gradient descent method to solve the inverse problem described in this paper, but because of space limitations, the parallel implementation will be described in a separate publication.

4. Numerical Experiments. In this section we present some numerical results to show the effectiveness of our *spectral* reconstruction method on real data taken of phantom breast objects with known materials. Specifically, we used two different phantom objects, one with homogeneous background material that allows for quantitative evaluation of image reconstruction quality, and another phantom with heterogeneous background material that provides a more realistic representation of actual breast tissue.

Projection images of these objects were acquired using a clinical breast tomosynthesis system (Selenia Dimensions, Hologic Inc.) used exclusively for research. This system acquires 15 projections over a 15 degree angular range, and reconstructs the imaged volume using the filtered backprojection (FBP) algorithm. FBP is often used in commercial systems because it is a well-understood method, and because it solves

the linear approximation (monoenergetic) model, it computes reconstructions very quickly.

To compare the obtained reconstructions of our spectral algorithm with the FBP reconstructions produced by the tomosynthesis system, the 2 or 3 separate material reconstructed images were combined to obtain one image representing the estimated linear attenuation coefficient of each voxel, and these were then transformed into *Hounsfield Units* (HU) [13].

4.1. Homogeneous Background Tissue. The first phantom we used consisted of four stacked semi-circular, 1 cm thick plates consisting of a homogeneous mixture of 50% breast adipose and 50% breast glandular tissue equivalent material with a fifth plate inserted in the center consisting of only adipose tissue equivalent material with nine 1 cm diameter holes throughout this plate. The nine holes were filled with 1 cm diameter targets consisting of different materials. For the images involving soft tissue lesions, six of the hole-filling targets consisted of an adipose-glandular tissue mixture with varying glandular-to-adipose ratios (0%:100%, 20%:80%, 40%:60%, ..., 100%:0%) with the remaining three holes being filled with other targets not used for analysis here. For the images involving microcalcifications, the targets consisted of 100% adipose material with added inserts representing calcium specks of multiple diameters (0.130, 0.165, 0.196, 0.230, 0.290 and 0.400 mm). This homogeneous phantom, due to its constant background, allows for simpler objective analysis of image quality by allowing for comparison between lesion signal and background.

Our spectral algorithm needed only 16 gradient descent iterations to get good reconstructed images. Further iterations did not improve the resolution, but it did increase the noise in the image. It is important to note that we currently do not have an automatic approach to choosing regularization parameters (in this case, the stopping iteration), and so our choice of stopping at iteration 16 was determined by experimentation.

Figure 4.1 shows an FBP reconstructed image (left) and a combined material reconstruction image (right) of the homogeneous phantom with the six homogeneous mixture inserts with varying glandular tissue mass fraction (% glandular mass fraction for each lesion is specified in the images). The seventh insert seen in the image was used only to fill in the hole and was not used in the present analysis. As can be seen, the contrast of the signals is not only improved by our spectral algorithm (right image), but also the increasing glandular density is better represented with our spectral reconstruction algorithm.

The signal difference-to-noise ratio (SDNR), a common image quality metric, was computed for each of the six signal inserts using the equation:

$$SDNR = \frac{\mu_{\text{signal}} - \mu_{\text{back}}}{\sigma_{\text{back}}}$$

where μ_{signal} and μ_{back} denote the mean of the voxel values in a region of interest (ROI) in the lesion and in the background (next to the lesion), respectively, while σ_{back} denotes the standard deviation of the background ROI. A graph of the SDNR vs. each lesion's known glandular fraction is shown in Figure 4.2, where it can be seen that our spectral reconstruction results in a larger increase in SDNR with lesion glandular fraction, improving visibility.

A zoomed-in version of the 100% glandular lesion are shown in Figure 4.3; vertical signal profiles (i.e., line slices) through the center of these lesions are shown in Figure 4.4. These figures demonstrate the improvement in homogeneity of our spec-
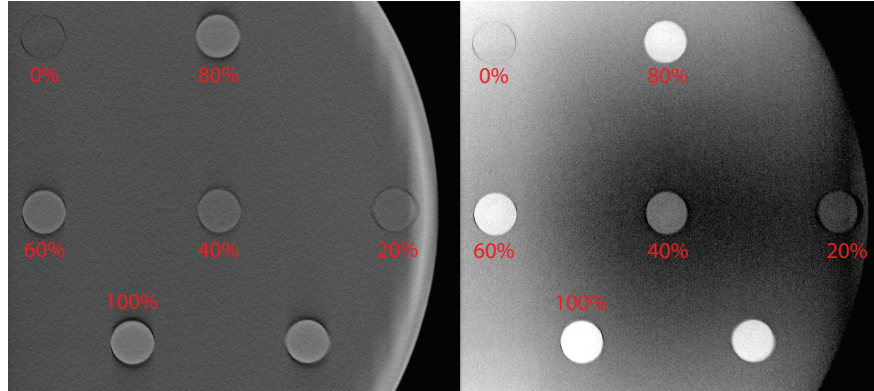
FIG. 4.1. *Reconstruction slices of a homogeneous phantom with six homogeneous mixture inserts. The left image is the FBP reconstruction produced by the tomosynthesis system, and the right image is the reconstruction produced by our spectral algorithm.*
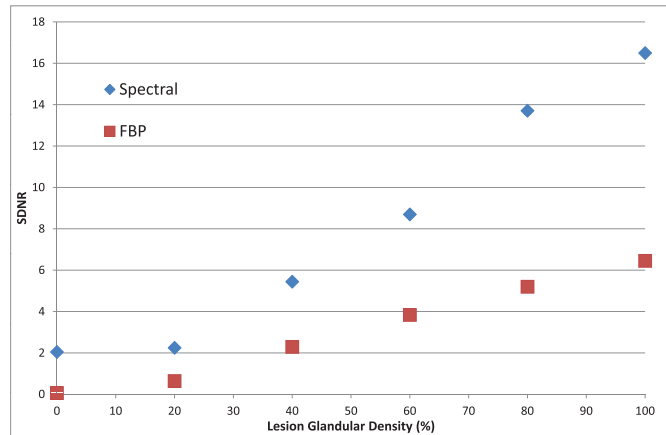

FIG. 4.2. *Plot of signal difference-to-noise ratio.*

tral reconstructed signal, compared to the distinct artifacts and cupping found in the FBP reconstruction.

Comparison of the obtained reconstructions when the microcalcification inserts were placed in the homogeneous phantom can be seen in the images in Figure 4.5, as well as the vertical signal profiles in Figure 4.6. In Figure 4.5, where the largest microcalcification cluster is shown, the large size of these high density signals introduces artifacts in the FBP reconstruction (left) (the dark regions above and below each speck, in the direction of the x-ray source motion), which are not present in our spectral reconstruction (right). Graphs of the corresponding vertical profiles through the center of the center speck, in addition to the vertical profile of the background next to the speck (see Figure 4.6) distinctly show the presence of the streak artifact. For these profiles, the voxel values of both the signal and background profiles for each reconstruction were normalized by subtracting the minimum value of the corresponding signal profile and then dividing by the maximum value. This allowed for a comparison between the two reconstruction algorithms using the same y-scale.

From these figures we can see that in the FBP reconstruction, the signal at the
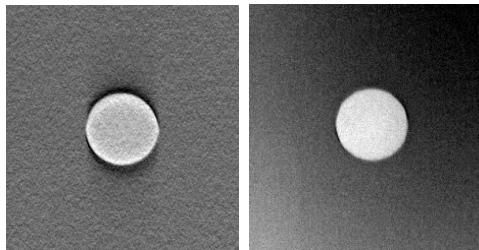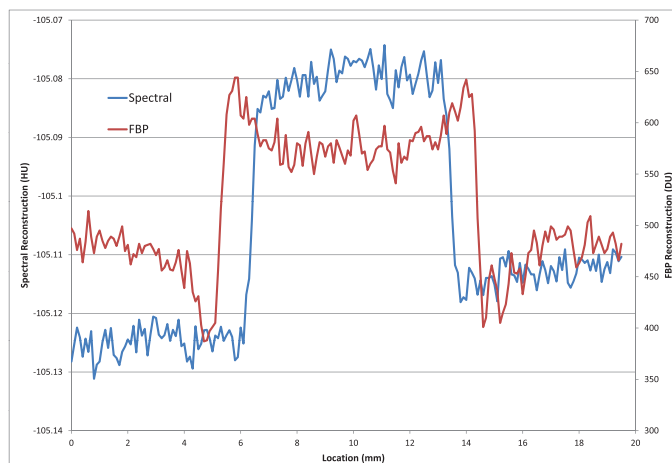
Fig. 4.3. *A zoom in on the 100% glandular lesion areas from Figure 4.1. The left image is the FBP reconstruction produced by the tomosynthesis system, and the right image is the reconstruction produced by our spectral algorithm.*

Fig. 4.4. *Vertical profile through the center of the images shown in Figure 4.3.*

microcalcification is lower than the background at least 1 mm from the center in each direction, while for our spectral reconstruction the signal matches the background almost immediately, with some slight (and narrower) reduction only present towards one side. It can also be seen from the graphs that the spectral reconstruction produces a narrower peak, representing improved spatial resolution. Figure 4.7 displays another pair of images showing a cluster with smaller microcalcifications. This figure shows somewhat improved visibility of the specks in our spectral reconstruction (right), with the left-most speck (indicated by an arrow in the figure) more visible compared to the FBP version (left).

4.2. Heterogeneous Background Tissue. The second phantom we used included the same 1 cm plate with holes and inserts as described in the previous subsection, but this time stacked in the center of four 1 cm thick plates with a heterogeneous mixture of adipose and glandular tissue equivalent materials. This phantom better tests the abilities of the tomosynthesis system and reconstruction algorithm due to the presence of overlapping signals, but in general only allows for qualitative evaluation, since with random structured backgrounds quantitative evaluation is challenging.

Images of the reconstructions of these heterogeneous phantoms are shown in Figure 4.8, which demonstrate that the improvements shown in the previous subsection can also be observed in these more challenging cases. Specifically, the more apparent
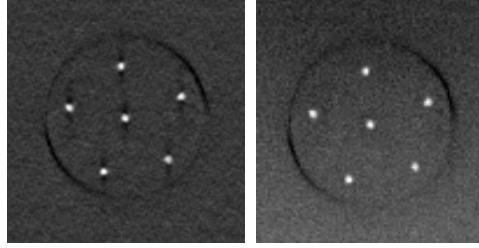
FIG. 4.5. *Comparison of microcalcification reconstructions. The left image is the FBP reconstruction produced by the tomosynthesis system, and the right image is the reconstruction produced by our spectral algorithm.*
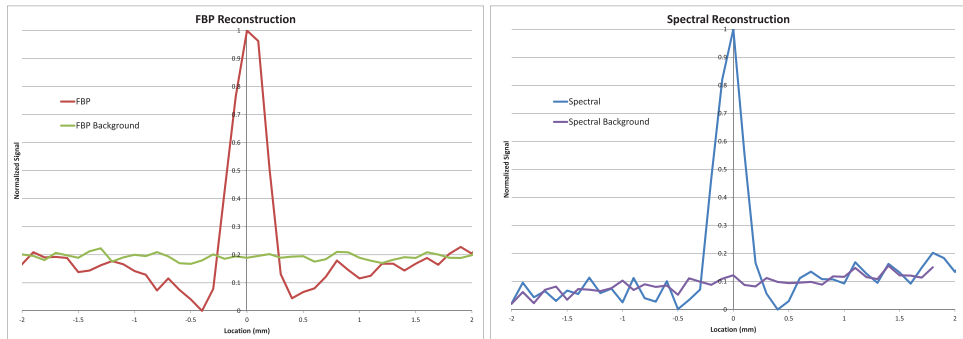

FIG. 4.6. *Comparison of line plots through the microcalcification reconstructions. The left image is the FBP reconstruction produced by the tomosynthesis system, and the right image is the reconstruction produced by our spectral algorithm.*

increase in contrast with increasing glandular fraction in the circular lesion signals (top) and the lack of streak artifacts in the microcalcifications (bottom) can be seen in our spectral reconstructions (right). We terminated our spectral reconstruction at 30 gradient descent iterations, when we observed stagnation in the decrease in the relative function values; see Figure 4.9.

5. Concluding Remarks. In this paper we described a nonlinear inverse problem for tomosynthesis image reconstruction that accurately models the polyenergetic nature of the x-ray beams, and that can incorporate knowledge about materials composing the object. Regularization was enforced by terminating the iteration. It is possible that explicit regularization methods, such as variational approaches, might be more effective. This is an important topic for future research.

The polyenergetic nature of the x-ray beams more accurately models the physics of the problem, while standard approaches such as FBP assume a monoenergetic x-ray beam. Thus, our spectral algorithm should, theoretically, produce better reconstructions than standard algorithms; the numerical experiments presented in this paper indicate that this is indeed the case. Moreover, we showed that iterative methods can be efficiently implemented by taking into account the various materials composing the object. The effectiveness of our spectral reconstruction algorithm was illustrated with real data taken of an object with known materials that simulates an actual breast.
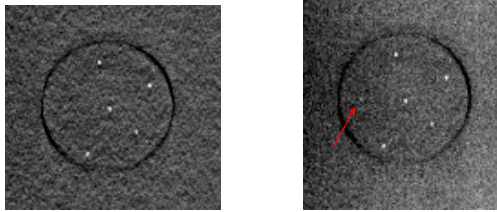
FIG. 4.7. *Comparison of a cluster of smaller microcalcification reconstructions. The left image is the FBP reconstruction produced by the tomosynthesis system, and the right image is the reconstruction produced by our spectral algorithm.*
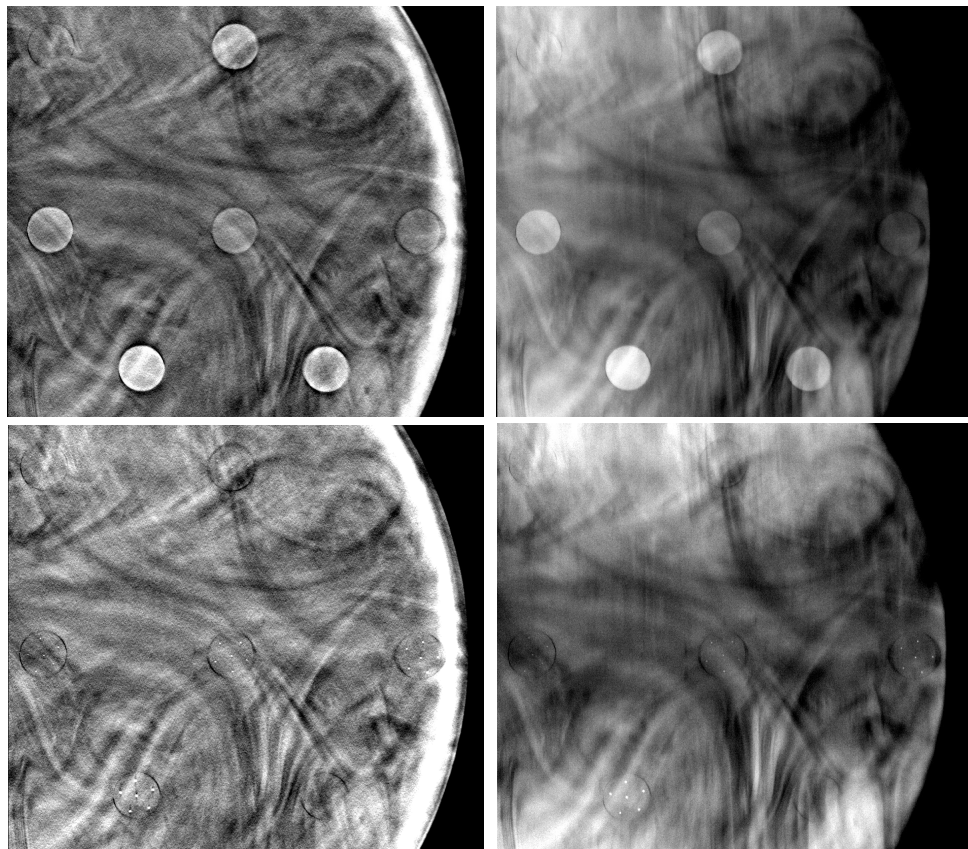

FIG. 4.8. *Reconstructions of the heterogeneous phantoms. The top row contains circular lesions of increasing glandular fraction, and the bottom row contains microcalcifications. The images on the left were obtained by FPB, and the images on the right were obtained by our spectral algorithm.*
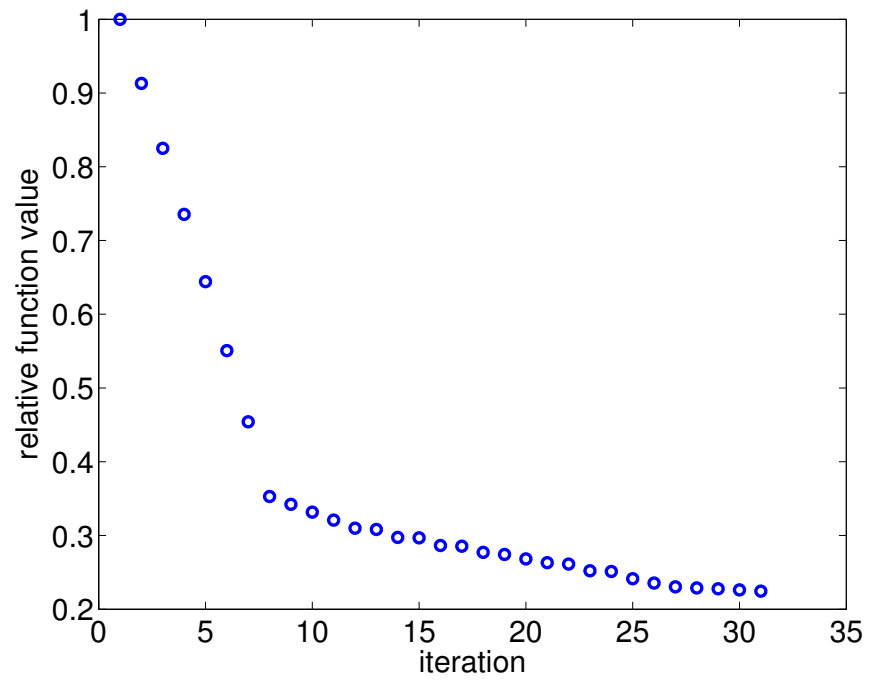
FIG. 4.9. *Plot of function values for the phantom object with heterogeneous background material.*

REFERENCES

[1] M. Bazalova, J. Carrier, L. Beaulieu, and F. Verhaegen, *Dual-energy CT-based material extraction for tissue segmentation in Monte Carlo dose calculations*, Phys. Med. Biol., 53 (2008), pp. 2439–2456.

[2] M. J. Berger, J. H. Bubbell, S. M. Seltzer, J. Chang, J. S. Coursey, R. Sukumar, D. S. Zucker, and K. Olsen, *XCOM: Photon Cross Sections Database*. National Institutes of Standards, 2009. http://http://www.nist.gov/pml/data/xcom/index.cfm.

[3] R. Brooks and G. Di Chiro, *Beam hardening in x-ray reconstructive tomography*, Phys. Med. Biol., 21 (1976), pp. 390–398.

[4] J. Chung, J. Nagy, and I. Sechopoulos, *Numerical algorithms for polyenergetic digital breast tomosynthesis reconstruction*, SIAM J. Imaging Sci., 3 (2010), pp. 133–152.

[5] K. Cranley, B. J. Gilmore, G. W. A. Fogarty, and L. Desponds, *Catalogue of Diagnostic X-Ray Spectra & Other Data*, Institute of Physics and Engineering in Medicine, York, 1997.

[6] B. De Man, J. Nuyts, P. Dupont, G. Marchal, and P. Suetens, *An iterative maximum-likelihood polychromatic algorithm for CT*, IEEE Trans. Med. Imaging, 20 (2001), pp. 999–1008.

[7] J. T. Dobbins and D. J. Godfrey, *Digital x-ray tomosynthesis: current state of the art and clinical potential*, Phys. Med. Biol, 48 (2003), pp. R65–R106.

[8] I. A. Elbakri and J. A. Fessler, *Statistical image reconstruction for polyenergetic x-ray computed tomography*, IEEE Trans. Med. Imaging, 21 (2002), pp. 89–99.

[9] ———, *Segmentation-free statistical image reconstruction for polyenergetic x-ray computed tomography with experimental validation*, Phys. Med. Biol., 48 (2003), pp. 2453–2477.

[10] H. W. Engl, M. Hanke, and A. Neubauer, *Regularization of Inverse Problems*, Kluwer Academic Publishers, Dordrecht, 2000.

[11] H. W. Engl and P. Kügler, *Nonlinear inverse problems: Theoretical aspects and some industrial applications*, in Multidisciplinary Methods for Analysis Optimization and Control of Complex Systems, V. Capasso and J. Périaux, eds., Springer, Berlin, 2005, pp. 3–48.

[12] H. W. Engl, K. Kunisch, and A. Neubauer, *Convergence rates for Tikhonov regularisation of nonlinear ill-posed problems*, Inverse Problems, 5 (1989), pp. 523–540.

[13] C. L. Epstein, *Introduction to the Mathematics of Medical Imaging, Second Edition*, SIAM, Philadelphia, PA, 2007.

[14] J. Noh, J. A. Fessler, and P. E. Kinahan, *Statistical sinogram restoration in dual-energy CT for PET attenuation correction*, IEEE Trans. Med. Imaging, 28 (2009), pp. 1688–1702.

[15] E. Y. Sidky, L. Yu, X. Pan, Y. Zou, and M. Vannier, *A robust method of x-ray source spectrum estimation from transmission measurements: Demonstrated on computer simulated, scatter-free transmission data*, J. Applied Physics, 97 (2005), pp. 124701–1:124701–11.

[16] C. R. Vogel, *Computational Methods for Inverse Problems*, SIAM, Philadelphia, PA, 2002.

[17] Y. Zhang, H.-P. Chan, B. Sahiner, J. Wei, M. M. Goodsitt, L. M. Hadjiiski, J. Ge, and C. Zhou, *A comparative study of limited-angle cone-beam reconstruction methods for breast tomosynthesis*, Med. Phys., 33 (2006), pp. 3781–3795.